Journal of Mining and Environment (JME) Vol. 17, No. 2, 2026, 447-467

Shahrood University of Technology

Journal of Mining and Environment (JME)

Journal homepage: www.jme.shahroodut.ac.ir

Iranian Society of Mining Engineering (IRSME)

Environmental impact mitigation of nickel mining activity – Case study in Central Sulawesi, Indonesia

Asep Nurohmat Majalis[1*], Muhammad Razzaq Al Giffari[2], R Arif Suryanegara[2], M Rifat Noor[3], Rachmat Ramadhan[4], and Noviarso Wicaksono[3]

1. Research Center for Chemistry, National Research and Innovation Agency, South Tangerang-Banten, Indonesia
2. Research Center for Environmental and Clean Technologies, National Research and Innovation Agency, South Tangerang-Banten, Indonesia
3. Research Center fot Mineral Technology, National Research and Innovation Agency, Tanjung Bintang-Lampung, Indonesia
4. National Research and Innovation Agency, Jakarta, Indonesia

Article Info

Received 19 May 2025

Received in Revised form 7 August 2025

Accepted 9 November 2025

Published online 9 November 2025

DOI: 10.22044/jme.2025.16265.3158

Keywords

Mining environmental impact management

Infiltration, Surface runoff coefficient

Sediment load

Chromium hexavalent

Abstract

Due to its large nickel reserves, Indonesia has become one of the world's largest nickel mining sites and producers. Nickel is a mining commodity with high economic value. However, its mining activity can negatively impact the environment if not managed properly. Therefore, mitigation of the impact of nickel mining is necessary. This research has conducted erosion and infiltration tests at various locations in pre-nickel mining sites to mitigate the environmental impact of nickel mining activity. Erosion tests were performed using a rainfall simulator with five nozzles on a 12.5 m² demo plot. Infiltration tests were conducted using a double-ring infiltrometer. The result shows that surface runoff coefficients for disposal, limonite, saprolite, and quarry sites were higher than those for vegetated sites such as grassland, pepper plantation, and forest. The saprolite site released the highest sediment load, i.e., 484.3 kg ha-1 hour-1, followed by the limonite and the pepper plantation site, with 243.6 kg ha-1 hour-1 and 185 kg ha-1 hour-1. The highest Cr(VI) concentration, 0.7 mg L-1, was released from the disposal site, followed by the saprolite, limonite, and pepper plantation sites, with concentrations of 0.56, 0.06, and 0.06 mg L-1, respectively. The infiltration equation obtained from each site shows that revegetation can significantly reduce runoff. Therefore, revegetation should be prioritized in addition to end-of-pipe treatment to mitigate the impact of nickel mining activities.

1. Introduction

Indonesia's abundant nickel ore reserves, particularly in islands such as Sulawesi, Obi, and Halmahera, have positioned the country as a strategic destination for global investment in lateritic nickel mining [1]. These islands, characterized by extensive ultrabasic bedrock formations, host the largest lateritic nickel deposits globally [2]. Driven by the surging demand for electric vehicle batteries—particularly lithium-ion batteries with NMC (nickel, manganese, cobalt) cathodes—nickel has emerged as a critical commodity. It has catalyzed substantial growth in mining and processing activities across Indonesia, especially in Sulawesi and Halmahera. Major industry players, including Vale and Antam, as well as industrial parks such as IMIP (Indonesia Morowali Industrial Park) and IWIP (Indonesia Weda Bay Industrial Park), are actively operating in these regions. By 2023, over 30 nickel ore processing companies were operational, with an additional 20 under development [3,4].

The rapid expansion of nickel mining has raised considerable environmental and social concerns. Conflicts with local communities have arisen due to land encroachment and environmental degradation, which encompasses biodiversity loss, contamination of surface and groundwater, soil degradation, and sedimentation of aquatic systems [5,6]. Mining activities frequently compromise air quality, human health and safety, and the local ecology [7]. The predominant nickel mining method, open-pit mining, results in vegetation loss,

Corresponding author: asepnurohmatmajalis@gmail.com (A. N. Majalis)

topsoil removal, and overburden extraction, which alters land cover and increases surface runoff [8–11]. Rainfall intensity, slope, and changes in land use influence runoff [12], with higher levels observed in open or disturbed areas compared to vegetated regions [12,13]. The increased surface runoff leads to erosion, sediment transport, and the mobilization of heavy metals, particularly hexavalent chromium (Cr(VI)). Cr(VI), originating from the oxidation of chromium-bearing ultramafic minerals, is characterized by its water solubility, high toxicity, and environmental persistence. The mobility of chromium in surface runoff, especially in oxy-anion forms (CrO_4^{2-}, $HCrO_4^-$, $Cr_2O_7^{2-}$), along with its carcinogenic and mutagenic properties, renders it a significant pollutant of concern [14–19]. Chromium (VI) concentrations are often increased in runoff from nickel mining, particularly in saprolite areas exhibiting considerable surface disturbance.

A systematic study is urgently needed to investigate the hydrological responses of various land cover types, focusing on erosion and infiltration assessments in a planned nickel mining area, to anticipate and mitigate environmental impact risks. In this study, field-based erosion tests utilizing a rainfall simulator were performed across stratified land cover sites, including forest, grassland, pepper plantations, saprolite, limonite, disposal, and quarry sites, to quantify runoff coefficients, sediment loads, and Cr(VI) concentrations. The parameters are essential for the design of sedimentation and tailing ponds, specifically in assessing their capacity, treatment functions, and maintenance schedules. In addition to the erosion assessments, infiltration tests utilizing double-ring infiltrometers were conducted to assess the water absorption capacity of the soil at each site. The infiltration rate is a critical measure of land hydrological resilience, influencing the capacity for rainfall retention and the subsequent decrease in surface runoff. Research indicated that vegetated sites demonstrated elevated infiltration rates, attributed to enhanced soil porosity and hydraulic conductivity resulting from root systems and organic matter [20–26]. The dynamics are crucial for hydrological restoration and for the development of effective reclamation and post-mining land rehabilitation strategies. This study establishes a comprehensive baseline for environmentally responsive mining planning by integrating erosion metrics, infiltration behavior, and pollutant mobility across various land covers. The findings highlight the importance of adopting differentiated management strategies tailored to specific land cover characteristics, thereby promoting more sustainable nickel mining practices in Indonesia.

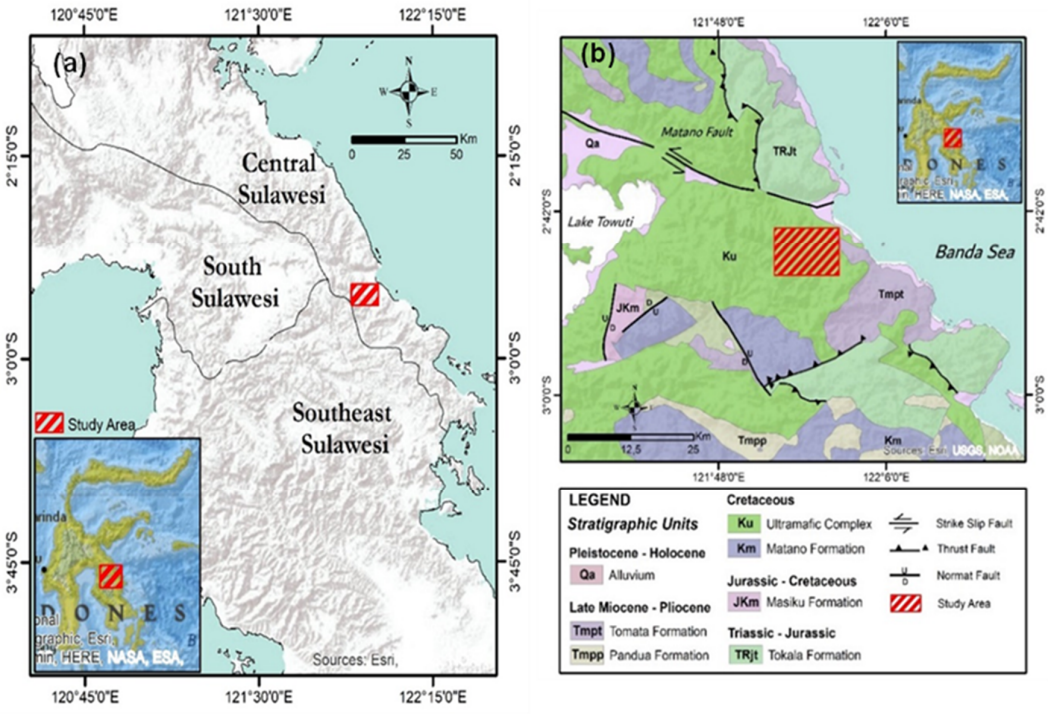

Figure 1. The study area (a), and the study area's geological map (b)

2. Materials and methods

2.1. Study area

This research was conducted in Bahodopi, Central Sulawesi Province, bordering the South Sulawesi and Southeast Sulawesi Provinces, as shown in Figure 1(a). The study area falls within the Eastern Sulawesi Ophiolite Belt [27]. This belt comprises mafic and ultramafic rocks, as well as sedimentary rocks, forming a mélange [28]. Additionally, Sulawesi exhibits complex tectonics, including the Matano Strike-Slip Fault near the study area, contributing to its undulating hilly morphology [29]. The study area predominantly comprises Cretaceous complex ultramafic rocks, extending northwestward and overlying the Masiku and Tokala Formation. The ultramafic complex comprises various rock types, including harzburgite, lherzolite, wehrlite, websterite, serpentinite, dunite, diabase, and gabbro. Nickel deposits develop in ultrabasic rocks such as dunite, peridotite, and serpentinite through lateritization processes [30]. Characterization of the lateritic nickel profiles in the Bahodopi area has been previously conducted [31], revealing that the lateritic nickel deposits originate from harzburgite and websterite rocks. Figure 1(b) shows the study area's geological map.

Bahodopi experiences a tropical climate, resulting in distinct rainy and dry seasons, typical of other regions in Indonesia. The peak of the rainy season occurs from April to June, with rainfall reaching up to 276 mm per month. Meanwhile, the dry season typically spans from August to October, with minimum monthly rainfall ranging from 56 to 108 mm. The average air temperature recorded at the Morowali station ranges from 27°C to 28°C. Like the study area, regions with tropical climates are conducive to laterite formation [32]. However, lateritic nickel formed from ultramafic rocks is a geogenic source of Cr(VI) [33]. Cr(VI) is hazardous to the environment due to its water solubility and toxicity to living organisms [34]. Hence, careful mining planning, such as conducting pre-mining erosion simulations, is essential to prevent environmental degradation.

2.2. Erosion test

The erosion test was conducted using a rainfall simulator, with five nozzle units, where a pump with adjustable flow rates controlled the rainfall intensity. The calibration and validation of rainfall simulators are critical to ensure they closely replicate natural rainfall conditions and produce reliable data in erosion studies. Calibration typically involves adjusting nozzle types and water pressure or height to control drop size and fall velocity—key parameters that influence raindrop kinetic energy and subsequent soil detachment. Research shows that realistic rainfall simulation is achieved when drops are approximately 2–3 mm in diameter and fall at near-terminal velocities of about 9 ms^{-1}, mimicking the natural impact of rain [35,36]. Rainfall intensity is measured and adjusted using evenly distributed rain gauges or collection trays across the experimental plot to maintain uniform coverage. Moreover, to standardize pre-test soil conditions and minimize variability in infiltration rates, the soil is often pre-wetted either by full soaking a day in advance or by applying a light artificial rain several hours prior to testing. These practices help align test conditions with realistic field scenarios, thereby increasing the reproducibility of results.

Despite these strengths, rainfall simulators have inherent limitations. Their small-scale application means findings are most useful for comparative trials rather than for direct extrapolation to landscape-scale hydrological modeling. Simulators are also sensitive to external disturbances, particularly wind, which can distort drop trajectories and require the use of shielding structures that may limit mobility [35]. Furthermore, due to height constraints, simulated drops may not reach full terminal velocity, potentially underestimating splash detachment and erosion intensity. Simulators typically generate rainfall at constant rates, limiting their ability to replicate the variability, intensity bursts, and duration patterns of natural storm events [36]. Lastly, field deployment can be logistically demanding, requiring a stable water supply, pumps, and maintenance, especially in remote terrain. Taken together, these constraints underscore the importance of interpreting rainfall simulator data cautiously, understanding that while they provide valuable insights into process dynamics under controlled conditions, they do not fully capture the complexity of natural rainfall–runoff–erosion interactions.

River water with characteristics presented in Table 1, analyzed using ICP-OES, was used for the erosion test. The area of the demo plot simulator was 12.5 m^2, which had a slope ranging from 7 to 10 degrees, reflecting the natural field conditions commonly found in nickel mining areas. The testing was performed at 2-day intervals, with each day comprising 3 hours of experiment. Observations and recordings of rainfall intensity and surface water runoff from the demo plot were

conducted every hour. This experimental design was based on widely accepted protocols in soil erosion and hydrological studies, where multi-hour simulations are necessary to capture the whole progression of infiltration, runoff initiation, steady-state flow, and sediment transport processes. Specifically, the 3-hour duration aligns with practices observed in in-situ rainfall simulation studies, such as those ref [37] and [24], which demonstrate that 2–4 hour durations are sufficient to observe both the early and mature stages of surface runoff dynamics.

Table 1. The water characteristics used in erosion test

Parameter	Class 1st Standard*	Unit	Result
Physical properties			
Color	15	Pt-Co Unit	<5
Total dissolved solid	1000	mg L^{-1}	88
Total suspended solid	40	mg L^{-1}	<0.5
pH	6-9		8.39
Metals			
Chromium hexavalent (Cr(VI))	0.05	mg L^{-1}	<0.01
Mercury (Hg)	0.001	mg L^{-1}	<0.0005
Manganese (Mn)	0.1	mg L^{-1}	<0.005
Boron (B)	1	mg L^{-1}	0.0209
Iron (Fe)	0.3	mg L^{-1}	0.0862
Cobalt (Co)	0.2	mg L^{-1}	<0.001
Nickel (Ni)	0.05	mg L^{-1}	<0.005
Copper (Cu)	0.02	mg L^{-1}	<0.005
Zinc (Zn)	0.05	mg L^{-1}	0.0082
Arsenic (As)	0.05	mg L^{-1}	<0.001
Selenium (Se)	0.01	mg L^{-1}	<0.005
Cadmium (Cd)	0.01	mg L^{-1}	<0.001
Barium (Ba)	1	mg L^{-1}	<0.001
Lead (Pb)	0.03	mg L^{-1}	<0.005

**Water quality standard refers to Appendix VI of the Government Regulation of Indonesia No.22 of 2021 about Implementation of Environmental Protection and Management*

The 2-day interval between tests was selected to allow partial recovery of soil moisture and minimize cumulative saturation effects that could bias the infiltration and erosion behavior in subsequent trials. This approach is consistent with findings by ref [23], which emphasize the importance of recovery time between infiltration events to restore near-field baseline hydrological conditions. Additionally, this interval facilitates the logistical preparation of equipment and ensures accurate, repeatable measurements. During each test, observations and recordings were conducted hourly, capturing data on rainfall intensity and the volume of surface runoff generated from the demo plot. These data were essential for calculating the surface runoff coefficient, sediment load, and analyzing Cr(VI) transport behavior under controlled rainfall conditions.

The surface runoff from the demo plot was then sampled to analyze the total suspended solids (TSS) and Cr(VI). The surface runoff coefficient and sediment load were calculated using Equations 1 and 2 as follows:

$$I = \frac{V}{R_f \times A} \quad (1)$$

Where are:

I – runoff coefficient

V – surface runoff volume generated from the demo plot area (L)

R_f – rainfall intensity (mm or L m^{-2})

A – demo plot area (m^2)

$$S_L = \frac{V \times TSS}{A \times t \times 100} \quad (2)$$

Where are:

S_L – sediment load (kg ha^{-1} $hour^{-1}$)

V – the surface water volume exiting the demo plot area (L)

TSS – total suspended solids (mg L^{-1})

A – demo plot area (m^{-1})

t – time (hour)

2.3. Infiltration test

The infiltration capacity of soils under various land cover types was evaluated using a double-ring infiltrometer, following established protocols

described by ref [38] and [20]. The apparatus consisted of two concentric metal rings, 50 cm in height, with diameters of 30 cm (inner ring) and 60 cm (outer ring). Water was added simultaneously into both rings to isolate vertical infiltration in the inner ring by minimizing lateral flow. Water level decline in the inner ring was recorded at fixed intervals (minutes): 0, 1, 2, 3, 4, 5, 6, 7, 8, 9, 10, 15, 20, 25, 30, 35, 40, 60, 80, 100, 120, 140, 160, 180, 200, and continued until the infiltration rate approached a steady-state.

To standardize initial soil conditions and minimize measurement variability, all test sites were ensured to be neither wet/saturated nor overly dry. Next, rings were inserted to a consistent depth of approximately 10 cm into the soil, following the guidelines of ref [39] and [40] to avoid preferential lateral flow or surface conformity. Infiltration testing sites were carefully selected to represent typical micro-environments within each land cover class. Plots with visible cracks, root interference, depressions, or signs of animal disturbance were excluded to reduce spatial variability. Tests were conducted on level ground or consistent slopes within each site to minimize the confounding effects of topography on infiltration rates [41]. Soil texture and surface condition were noted qualitatively for further interpretation.

Infiltration rate and cumulative infiltration depth were sequentially calculated using Equations 3 and 4 as follow:

$$f_c = \frac{\Delta h}{\Delta t} \quad (3)$$

Where are:

f_c – the infiltration rate (cm minute^{-1})

Δh – the water decline in the inner ring of the infiltrometer (cm)

Δt – the time interval (minute)

$$CI = \sum \Delta h \quad (4)$$

Where are:

CI – the cumulative infiltration depth (cm)

Δh – the water decline in the inner ring of the infiltrometer (cm)

Subsequently, the resulting infiltration curves and cumulative depth data were analyzed to characterize infiltration behavior and saturation trends, and then compared with empirical models, such as the Kostiakov equation, for comparative analysis among land cover types.

2.4. Suspended solid and (Cr(VI) analysis

Suspended solid analysis was conducted using the photometric method with a Hach DR890 spectrophotometer. Approximately 500 mL of surface runoff samples obtained from erosion testing were blended at high speed for 2 minutes using a blender. The blending process aimed to homogenize and break down soil particle sizes carried by surface runoff into finer particles, preventing easy sedimentation during measurement. The blended sample was then poured into a 1000 mL beaker, mixed until homogeneous, and immediately, 25 mL of the sample was poured into the Hach DR890 sample cell. The suspended solid is analyzed on the Hach DR890 at wavelength 860 nm with distilled water as the blank.

The analysis of Cr(VI) was conducted using the 1,5-diphenylcarbohydrazide method. Approximately 20 mL of surface runoff samples obtained from erosion testing were filtered to obtain clean water samples. Furthermore, 10 mL of the filtered sample was poured into the Hach DR890 sample cell, and one packet of Chroma Ver 3 reagent powder was added. The cell was closed and inverted several times to mix the reagent and sample. The reaction process was allowed to proceed for 5 minutes. A purple color would form if Cr(VI) were present in the sample. The Cr(VI) concentration was measured on the Hach DR890 spectrophotometer at wavelength 540 nm with distilled water as the blank.

2.5. Land cover change mapping and runoff coefficient recalculation

To evaluate the hydrological implications of land-use transformation due to nickel mining, a land cover change analysis was conducted at the sub-watershed scale. The initial land cover prior to mining activities was established through visual interpretation of satellite images from Google Earth, supported by field observations and photo documentation during fieldwork [4]. Land cover classes were categorized into forest, shrubland, plantation, saprolite, limonite, disposal, quarry, rice field, and built-up areas, based on vegetation structure, color signature, and topographic characteristics. This classification served as the basis for assessing pre-disturbance hydrological conditions in each sub-watershed.

The post-mining land cover distribution was derived from spatial simulation. This scenario-based land use map reflects the anticipated surface disturbance associated with full-scale mining

operations, including the expansion of saprolite extraction areas and the placement of overburden disposal sites. The simulation was georeferenced and harmonized with the pre-mining map to enable pixel-by-pixel comparison and area-based quantification of land cover transitions. The resulting change matrix allowed identification of critical shifts in land cover composition within each sub-watershed.

To estimate the hydrological consequences of these land cover changes, runoff coefficients were recalculated using a composite area-weighted method. Each land cover type was assigned a representative runoff coefficient value, informed by field-based erosion and infiltration tests conducted using rainfall simulators and double-ring infiltrometers [42]. These values ranged from 0.05 for undisturbed forest to 0.85 for highly compacted disposal sites. The composite runoff coefficients (Cro) for each sub-watershed were computed by multiplying the areal proportion of each land cover class by its corresponding runoff coefficient value, both before and after mining. This approach enabled a quantitative comparison of runoff potential across time and space, providing insight into how landscape-scale land disturbance translates into an escalation of hydrological risk.

3. Results and discussion

This study primarily conducted erosion tests using a rainfall simulator and infiltration tests using a double-ring infiltrometer. Both tests were performed on seven distinct land cover types, namely forest, grassland, pepper plantation, limonite, saprolite, disposal, and quarry sites. These categories were selected to represent the full spectrum of ecological and operational conditions present across the mining concession. The selection of test plots was based on a detailed land cover classification map generated from recent satellite imagery, which was cross-verified with ground-truthing observations.

Each site was chosen to reflect a typical condition of the respective land cover type in terms of vegetation density, surface disturbance, slope, and proximity to runoff flow paths. This approach ensures that the measured responses to rainfall and infiltration represent the broader hydrological behavior of the mining landscape. Similar sampling frameworks have been adopted in erosion studies in mining areas, where stratified land cover-based sampling increases ecological validity and spatial generalization [43,44].

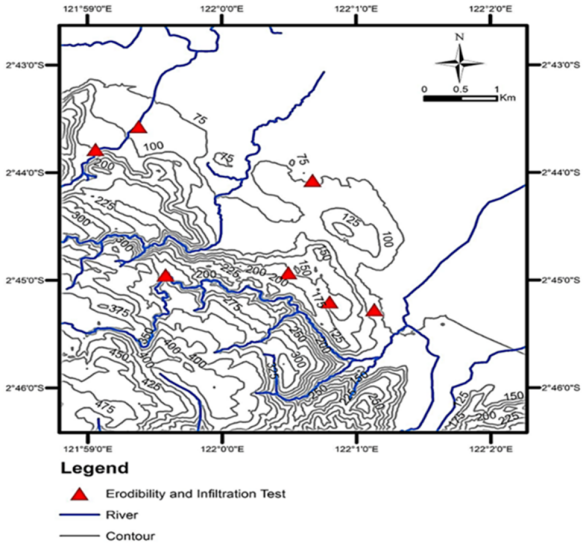

Figure 2. Erosion and infiltration test location

Figure 3. Erosion and infiltration test activity

The chosen sites collectively encompass both natural (e.g., forest, grassland) and disturbed mining surfaces (e.g., saprolite, quarry, disposal), capturing variation in soil compaction, surface sealing, and vegetation cover—all of which significantly influence erosion and infiltration behavior. This stratified selection framework enables a robust interpretation of how land cover changes induced by mining activities affect the hydrological response. The location maps for the erosion and infiltration tests are shown in Figure 2, while the test activities are illustrated in Figure 3.

3.1. Surface runoff coefficient, sediment load, and Cr(VI) release

The erosion test was designed to simulate the transformation of raindrops into surface runoff and quantify the associated sediment transport. As rainfall interacts with exposed soil surfaces, part of the water infiltrates, while the rest forms surface runoff that mobilizes soil particles, contributing to erosion and sediment deposition downslope. The hydrological response varies across land cover types, influencing the rates of infiltration, runoff, and sediment transport.

The rainfall simulator employed in this study utilized five nozzle units to generate artificial rainfall over a 12.5 m² test plot with a slope gradient of 7–10 degrees. The design of rainfall simulators varies, from compact models with a 6-inch spray area to larger systems covering up to 4.5 × 22 meters [45]. Despite design differences, key performance criteria include ease of construction, adaptability to field conditions, affordability, capacity to deliver uniform rainfall, and consistent water supply [37]. In this test, two rainfall intensities were applied for a duration of three hours each. Surface runoff was channeled through a steel lip embedded at the lower edge of the test plot and collected in drums. Water samples were taken hourly to measure suspended sediment load and Cr(VI) concentrations. These data were subsequently used to calculate runoff coefficients and were integrated with infiltration test results for cross-validation.

Analysis of the erosion test revealed that open land cover types exhibited significantly higher runoff coefficients than vegetated sites. As shown in Table 2, the disposal site recorded an average runoff coefficient of 0.44 on day 1, rising sharply to 0.80 on day 2. The accumulation of soil moisture attributed this increase, as rainfall declined from 24.17 mm hour^{-1} on day 1 to 17.67 mm hour^{-1} on day 2. Despite lower rainfall on the second day, runoff volume rose from 132.80 L hour^{-1} to 177.33 L hour^{-1}, indicating reduced infiltration capacity likely caused by soil saturation and the high clay content observed in the disposal area.

At the quarry site, a similar trend was observed. The runoff coefficient increased from 0.18 on day 1 to 0.65 on day 2, while rainfall dropped from 40 mm hour^{-1} to 17.67 mm hour^{-1}. The substantial increase in runoff despite reduced rainfall suggests that moisture retention in the upper soil layers limited infiltration into the more compact subsurface. Field observations also noted fine cracks in the quarry rocks, which may have partially facilitated water penetration despite overall compaction.

At the limonite site, the average surface runoff and runoff coefficient significantly escalated between the two testing days, rising from 118 L hour^{-1} and 0.23 on day one to 428.33 L hour^{-1} and 0.47 on day two. This increase aligns with a rise in rainfall from 41.5 mm hour^{-1} to 75.83 mm hour^{-1}, indicating an 82.7% increase in precipitation and a 104.3% increase in the runoff coefficient. The findings indicate that the increased moisture levels on day 2, together with the elevated clay mineral concentration at the limonite site, diminished infiltration and facilitated surface runoff, corresponding to the conditions reported at the disposal site.

At the saprolite site, the average surface runoff on day 1 was 391 L hour^{-1}, corresponding to a runoff coefficient of 0.39. On day 2, the average surface runoff decreased to 208 L hour^{-1}, with a runoff coefficient of 0.40. Despite a significant reduction in rainfall, from 87.33 mm hour^{-1} to 42.17 mm hour^{-1}, the runoff coefficient values exhibited minimal variation. This pattern indicates that soil moisture levels approached saturation, thereby restricting infiltration and maintaining surface runoff levels.

Runoff values at the pepper plantation site were significantly reduced. On day 1, the average runoff and runoff coefficient were 162.87 L hour^{-1} and 0.17, respectively, decreasing to 84.80 L hour^{-1} and 0.11 on day 2. During this period, rainfall decreased from 71.67 mm hour^{-1} to 59.67 mm hour^{-1}. The low runoff coefficient is due to cultivated soil conditions that improve porosity and infiltration. The results of the infiltration test corroborate this relationship and are consistent with the theoretical mass balance that categorizes rainfall into runoff, infiltration, and evaporation [46]. The relationship between infiltration and surface runoff coefficients is inversely

proportional; thus, land with enhanced infiltration capacity produces reduced runoff.

No surface runoff was observed at the grassland site on day 1, despite rainfall reaching 36.33 mm hour^{-1}. On day 2, as the soil approached saturation, runoff increased to 44.37 L hour^{-1}, exhibiting a runoff coefficient of 0.20, despite a decrease in rainfall to 17.67 mm hour^{-1}. The presence of dense grass covers enhanced porosity and initial infiltration; however, prolonged saturation resulted in delayed runoff formation.

Surface runoff was not observed at the forest site on either day, despite recorded rainfall levels of 36.17 mm hour^{-1} and 32.33 mm hour^{-1}. Extensive root networks contribute to high porosity, which effectively prevents surface water accumulation. This observation highlights the significant role of forested landscapes in reducing runoff and emphasizes the enduring effectiveness of reforestation efforts. Forest ecosystems function as natural hydrological buffers by absorbing, storing, and gradually releasing water. At all locations, excluding the forest, the runoff coefficient rose from day 1 to day 2, mainly due to the gradual saturation of the soil, which diminishes infiltration capacity and enhances surface runoff. Figure 4a-b presents the sequence of surface runoff coefficient values obtained from erosion tests conducted on day 1 and day 2.

Table 2. The surface runoff volume and surface runoff coefficient obtained from erosion test

Location/sites	Day	Time (hour)	Rainfall (mm)	Surface runoff (Liter)	Average of suspended solid released (mg L^{-1})
Disposal	1	1	22.5	68.5	225.76
		2	27	128.4	
		3	23	201.5	
	2	1	17.5	166	
		2	17.5	190	
		3	18	176	
Grassland	1	1	32	0	232.15
		2	40	0	
		3	37	0	
	2	1	17.5	0	
		2	17.5	56	
		3	18	77.1	
Quarry	1	1	38	17	394.50
		2	37	102.4	
		3	45	156.8	
	2	1	17.5	91.1	
		2	18	131.1	
		3	18	211.1	
Forest	1	1	37	0	0
		2	35	0	
		3	37	0	
	2	1	32	0	
		2	31	0	
		3	35	0	
Limonite	1	1	37	28	904.33
		2	49	124	
		3	39	202	
	2	1	85	375	
		2	85	450	
		3	58	460	
Pepper plantation	1	1	39	34.6	1580.83
		2	101	184	
		3	75.5	270	
	2	1	53	42.3	
		2	62.5	104	
		3	63.5	108.1	
Saprolite	1	1	88	221.5	1814.67
		2	59	451.5	
		3	116	501.5	
	2	1	42,5	212.3	
		2	43	207	
		3	41	206.3	

The saprolite site recorded the highest sediment load, followed by limonite, pepper plantation, quarry, disposal, and grassland sites, with respective values of approximately 453.69, 205.86, 79.42, 38.87, 24.98, and 12.88 kg ha^{-1} hour^{-1}. These figures correspond to rainfall intensities ranging from 20.92 to 65.67 mm hour^{-1}. No sediment load was detected in the forest site, even under a rainfall intensity of 34.25 mm hour^{-1} sustained for three hours over two consecutive days, further demonstrating the erosion control capability of forest cover. Sediment load values and the rainfall that stimulate them are presented in Figure 4c-d.

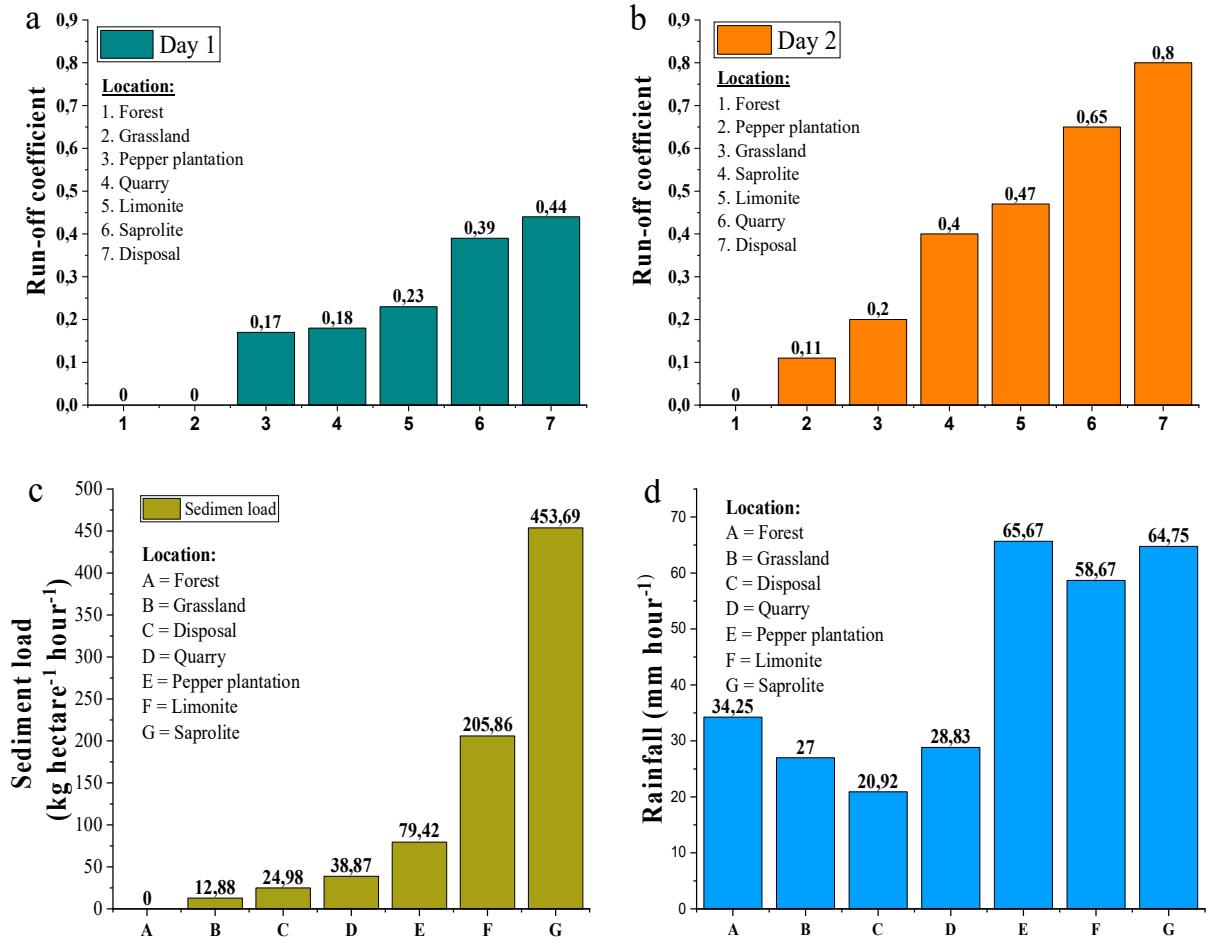

Figure 4. Surface runoff coefficient at observation sites in day 1 (a) and day 2 (b), sediment load released from observation sites (c), and rainfall poured down to the observation sites (d).

Land cover was a dominant factor influencing sediment load, especially in the forest and grassland sites. However, in sites such as the pepper plantation, rainfall intensity played a greater role. Other contributing factors include soil surface roughness [47], slope gradient [48,49], soil composition [24,49], and the amount of surface runoff [50]. Given that the saprolite, limonite, and pepper plantation sites contributed disproportionately to sediment transport, these areas should be prioritized in environmental management planning. Unmanaged sediment discharge from these sites poses significant risks to water bodies. Reforestation has shown significantly reducing sediment load, as shown in the forest site, and should be systematically integrated into both active and post-mining reclamation efforts. Complementary "end-of-pipe" interventions, such as sedimentation and tailing ponds, remain essential for mitigating downstream sedimentation risks.

Beyond sediment load, hexavalent chromium (Cr(VI)) represents a critical pollutant associated with surface runoff in nickel mining areas. Cr(VI)

is generated through the oxidation of chromium-bearing minerals in ultrabasic rocks, especially when exposed to air and ultraviolet radiation. Once formed, Cr(VI) dissolves readily in water and can be transported via surface runoff into surrounding water bodies. Its environmental and health hazards are substantial: Cr(VI) is highly toxic, mutagenic, and carcinogenic, with toxicity levels up to 100 times greater than trivalent chromium (Cr(III)) [17–19,51]. Its persistence in the environment, because of non-biodegradable properties, poses long-term risks to both ecosystems and human populations [33].

Ref [52] identified industrial effluents containing Cr(VI) and found ingestion, dermal absorption, and inhalation to be the main routes of human exposure to Cr(VI). Although direct human exposure from mine runoff is rare, indirect exposure through contaminated river systems used for drinking and bathing remains a serious concern. Each exposure pathway has different toxicological risks. Ref [53,54] noted that Cr(VI) can induce DNA damage in all routes of exposure through the formation of free radicals, which bind to genetic material. Inhalation and ingestion have explicitly been linked to increased carcinogenic outcomes.

The concentrations of Cr(VI) detected in surface runoff from erosion simulations in Bahodopi, Central Sulawesi, underscore this concern. As illustrated in Figure 5, the highest Cr(VI) concentration was observed in the disposal site (0.70 mg L^{-1}), followed by saprolite (0.56 mg L^{-1}), limonite and pepper plantation (each 0.06 mg L^{-1}), and quarry and grassland (each 0.01 mg L^{-1}). No detectable Cr(VI) release was observed at the forest site. These findings show that disturbed, unvegetated sites are primary sources of Cr(VI) pollution, whereas forested landscapes offer adequate protection through natural filtration and stabilization processes.

Notably, concentrations in the disposal, saprolite, limonite, and pepper plantation sites exceed the WHO drinking water threshold of 0.05 mg L^{-1}, posing potential health risks for local communities that lack water treatment infrastructure [55]. Cr(VI) contamination has profound implications for the integrity of the food chain. It can be absorbed by plants—accumulating in roots and causing nutrient imbalances and growth inhibition [56] — and kept by aquatic organisms such as fish and shrimp through bioaccumulation [57]. Top-level consumers in aquatic ecosystems, including humans, may ingest Cr(VI) through the consumption of contaminated fish, with bioaccumulation risks compounding over time. Larger and older aquatic organisms keep more Cr(VI), increasing potential human exposure. These dynamics underscore the urgency of implementing effective Cr(VI) mitigation strategies in nickel mining regions.

3.2. Infiltration

Field infiltration trials revealed significant variation in infiltration rates across the observed land cover sites. Vegetated sites, particularly forest and pepper plantation areas, exhibited higher initial infiltration rates compared to open sites. Specifically, infiltration rates in the forest and pepper plantation sites were 3.2 and 3.6 cm $minute^{-1}$, respectively, reflecting the influence of dense vegetative cover (Figure 6a). In contrast, lower rates were recorded in the quarry (2.0 cm $minute^{-1}$), grassland (1.0 cm min^{-1}), saprolite (0.3 cm $minute^{-1}$), limonite (0.3 cm $minute^{-1}$), and disposal (0.1 cm $minute^{-1}$) sites. Vegetation enhances infiltration by modifying soil hydraulic properties—such as reducing bulk density and increasing porosity—primarily through root activity [12,20,26].

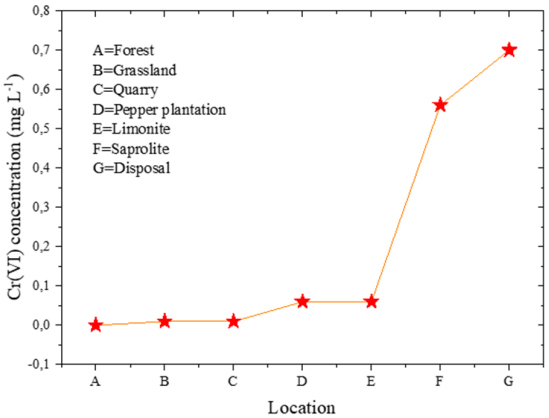

Figure 5. Cr(VI) concentration released from observation sites

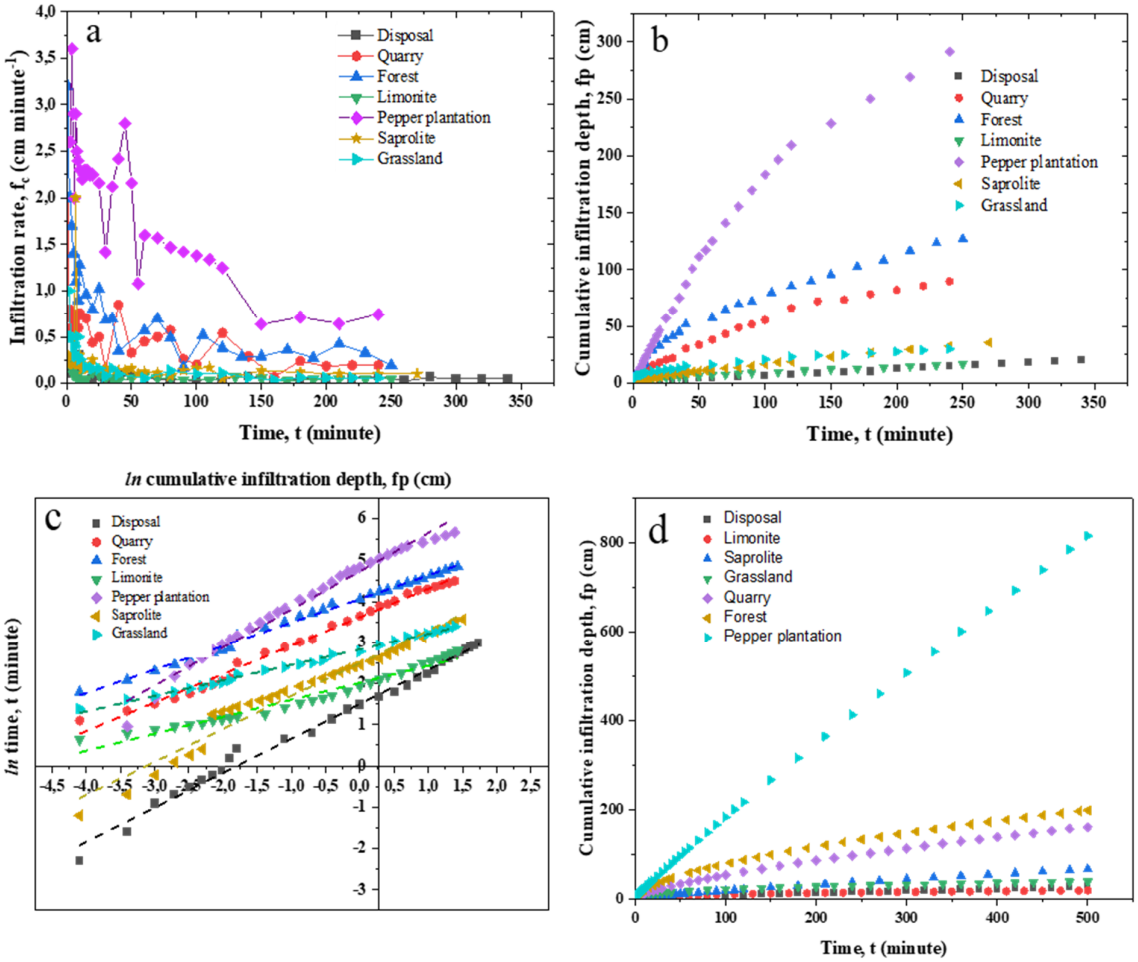

Figure 6. The changes in the infiltration rate as affected by time (a), the cumulative infiltration depth (b), the correlation of ln f_p vs ln t to obtain Kostiakov's equation (c), fitted infiltration data to Kostiakov's equation (d)

Figure 6a also demonstrates that the time required to approach soil saturation varied by site. While the forest and pepper plantation sites maintained a relatively constant infiltration rate throughout the trial period, the infiltration curves for the quarry, limonite, saprolite, and disposal sites flattened as they approached saturation. This plateau suggests limited infiltration capacity, likely due to the presence of swelling clay minerals, especially in the limonite and disposal sites. Such minerals impede water movement into deeper soil layers. Furthermore, soil texture plays a critical role: clay-rich soils retain water longer, delaying saturation, whereas sandy soils facilitate faster percolation [46]. Soils with high clay content generally exhibit lower infiltration capacity [58]. Additionally, observed mechanical compaction in the disposal area further reduced infiltration by increasing soil bulk density and decreasing porosity [59].

The infiltration rate is closely linked to cumulative infiltration depth—the total vertical distance that water travels into the soil. This metric reflects the combined effects of soil structure, porosity, and saturation. During the experiment, the decline in water level in the infiltrometer's inner ring was used to estimate the vertical infiltration depth. A faster rate of decline indicated higher infiltration and deeper percolation. The cumulative infiltration curves generated across all land cover types, as shown in Figure 6b, provide critical insights into the soil's water absorption dynamics under varying field conditions.

The pepper plantation site exhibited the most significant cumulative infiltration depth among all land cover types. This outcome is likely attributed to high soil porosity, which facilitates greater water retention and movement. In agricultural contexts, routine soil tillage enhances porosity, improving the soil's capacity to absorb and store both water and nutrients. Soil porosity is a key determinant of

infiltration depth; sandy soils, which possess larger pore spaces, allow water to percolate more deeply than clayey soils. It is plausible that the subsoil layer in the pepper plantation site contains a higher proportion of sand compared to other sites, contributing to its superior infiltration performance. Besides porosity, subsurface fractures or voids can significantly influence both the infiltration rate and the cumulative infiltration depth.

At the quarry site, field observations revealed many fine cracks within the rock matrix. These fractures, combined with relatively high sand content and inter-rock voids, facilitated a notable increase in water infiltration. The observed infiltration rate and cumulative depth of the quarry site exceeded those in the saprolite, limonite, and disposal sites, validating the influence of rock permeability and structural discontinuities. Under typical conditions, unfractured rock surfaces are less permeable than soil, suggesting that the infiltration enhancements in this site result from these physical anomalies.

Overall, multiple interrelated factors governed the magnitude of infiltration, including vegetation cover, soil texture and porosity, land use practices, surface roughness, organic matter content, and moisture levels [60]. The findings underscore the importance of both natural and anthropogenic factors in shaping infiltration dynamics, particularly in post-mining and reclaimed landscapes.

The data (Figure. 6b) are fitted to Kostiakov's infiltration rate model according to the Equation 5 [20], and to obtain the values of the soil characteristic parameters (M and n), the Equation 5 is transformed into a natural logarithm, yielding Equation 6.

$$I = M \times t^{n} \quad (5)$$

$$\ln I = \ln M + n \times \ln t \quad (6)$$

Where are:

I – the cumulative infiltration depth (cm)

M – the initial infiltration rate and soil structure conditions (cm minute^{-1})

t – time interval (minute)

n – the soil structure stability index

Subsequently, a linear regression analysis was conducted using the natural logarithmic form of Kostiakov's equation, plotting ln I against ln t (Figure 6c). The slope of the resulting linear fit provides the value of the soil structure stability index (n), while the intercept corresponds to ln M, which is then converted to M through an anti-log transformation. The derived parameters—M, n, the resulting infiltration equations, and corresponding R^2 values—are summarized in Table 3. The fitted infiltration models for each land cover site are graphically represented in Figure 6d.

Table 3. Kostiakov's equation obtained from field infiltration test

Location/sites	Kostiakov's Equation			
	M	n	Equation	R^2
Pepper plantation	113,64	0,93	$I = 113,64 (t^{0,93})$	0,98
Forest	58,03	0,58	$I = 58,03 (t^{0,58})$	0,99
Quarry	37,23	0,69	$I = 37,23 (t^{0,69})$	0,99
Grassland	17,04	0,38	$I = 17,04 (t^{0,38})$	0,99
Saprolite	12,06	0,80	$I = 12,06 (t^{0,80})$	0,96
Limonite	7,51	0,41	$I = 7,51 (t^{0,41})$	0,96
Disposal	4,48	0,84	$I = 4,48 (t^{0,84})$	0,99

The variability of M and n values across sites (M ranging from 4.48 to 113 and n from 0.38 to 0.93) reflects substantial differences in soil structure and infiltration behavior. These variations are primarily influenced by factors such as soil texture, vegetation cover, organic matter, moisture levels, and surface compaction. This observation is consistent with prior studies, which emphasize that infiltration rates are governed by physical soil properties including texture [20,24], moisture content [20,21,23,24], mineral composition [24], and structural integrity or compaction [22].

As shown in Figures 6a and 6b, the highest infiltration rates and cumulative infiltration depths were observed in the pepper plantation and forest sites. Both areas also exhibited the highest M values, affirming the positive correlation between M and infiltration capacity. Interestingly, the value was higher in the pepper plantation compared to the forest, suggesting a more rapid decline in the infiltration rate. It may be attributed to the less

stable soil structure in cultivated sites, where loosening may reduce long-term infiltration stability. Collectively, the M and n values for vegetated lands support the role of land cover in enhancing infiltration processes. These findings underscore the relevance of ecological rehabilitation in mining regions. In particular, implementing Concurrent Mining and Reclamation (CMR) practices has been shown to yield better ecological restoration outcomes than conventional Post-Mining Reclamation (PMR) approaches [61].

3.3. The correlation of surface runoff coefficient and infiltration

The data presented in Figure 7 demonstrate an inverse relationship between the infiltration rate, cumulative infiltration, and surface runoff coefficient. As infiltration capacity increases, the corresponding runoff coefficient decreases. Among the observed land cover types, the pepper plantation site exhibited the highest infiltration rate and cumulative infiltration, likely due to improved soil structure resulting from active land management. Despite this, a minor amount of surface runoff was still recorded, possibly because of intermittent saturation caused by clay-rich subsoil. The presence of clay increases soil impermeability, limiting water infiltration under high-moisture conditions [60].

In contrast, the disposal site exhibited the lowest infiltration rate and cumulative infiltration depth, coupled with the highest surface runoff coefficient. Field observations revealed evidence of significant soil compaction at this site, which contributes to reduced infiltration capacity. Soil compaction increases bulk density and reduces porosity, hindering water percolation into the subsurface and exacerbating surface runoff [59]. These findings underscore the significant role of soil physical properties in regulating hydrological responses across diverse mining-affected land cover types.

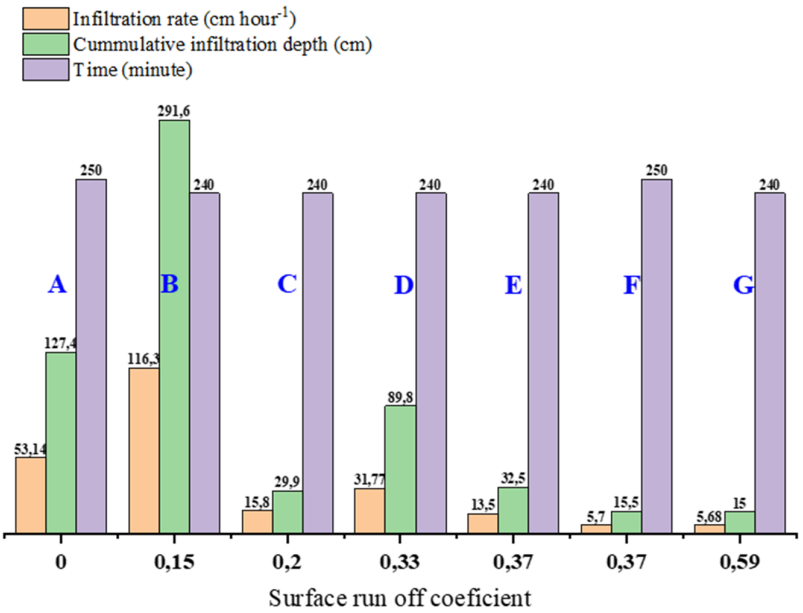

Figure 7. Surface runoff coefficient, infiltration rate, cumulative infiltration depth and total time from erosion and infiltration study results. A (forest), B (pepper plantation), C (grassland), D (quarry), E (saprolite), F (limonite), and G (disposal).

3.4. Watershed-scale land cover change and runoff coefficient recalculation

Understanding the hydrological impacts of land disturbance at the watershed scale is crucial for designing effective environmental mitigation strategies in mining-affected regions. While field-based erosion and infiltration assessments offer localized insights into hydrological behavior under varying land cover types, extrapolating these findings to broader spatial contexts necessitates integration with land cover change mapping.

In this study, a spatial analysis of pre- and post-mining land cover was conducted across six sub-watersheds in the Bahodopi mining area, Central Sulawesi. The comparison between pre-mining and post-mining land cover maps (Figure 8) illustrates substantial spatial transformation, particularly in

the central and southern portions of the concession area. Notably, large swathes of forest (in dark green) were replaced by saprolite sites (light brown), disposal areas (orange), and quarry sites (pink), all of which are characterized by reduced vegetation and increased surface sealing. This transformation reflects intensive land clearing and topsoil removal associated with nickel mining activities.

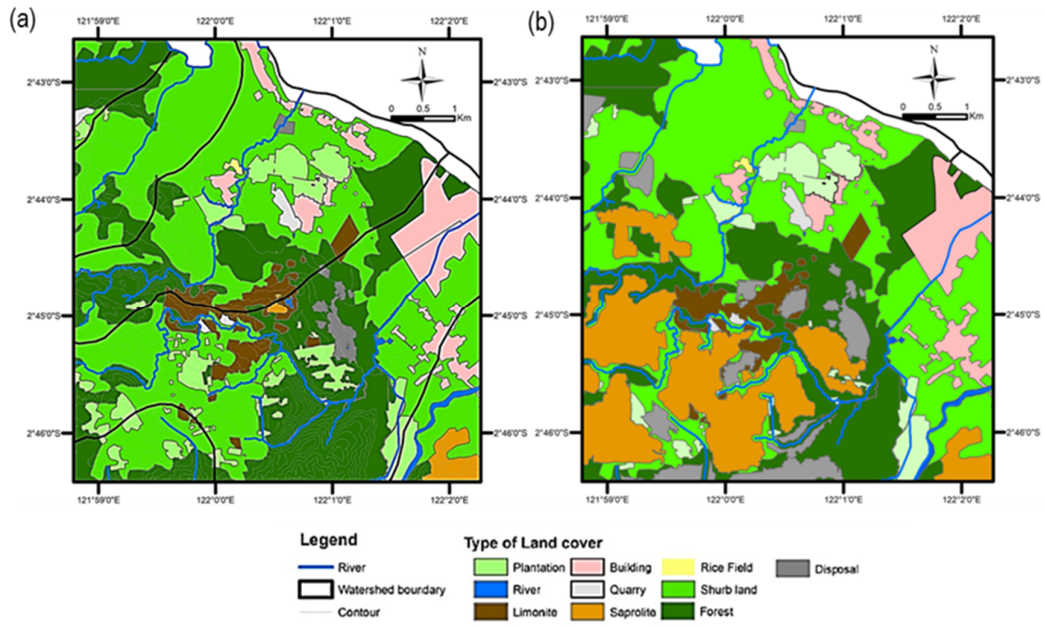

Figure 8. Land cover map. (a) pre-mining, and (b) post mining

Quantitative assessment of these land cover changes further reinforces the visual interpretation. As presented in Figure 9, forest area decreased across all sub-watersheds, with the most severe decline occurring in the Lamasara sub-watershed, where forest cover fell by over 23%. Similarly, shrubland and plantation areas declined by approximately 11% and 5%, respectively. In contrast, anthropogenically disturbed land types—particularly saprolite and disposal sites—showed significant expansion by 31% and 16%, respectively. These shifts show a systemic increase in imperviousness across the landscape, which is a known driver of enhanced surface runoff and reduced infiltration.

To evaluate the hydrological implications of these land cover modifications, area-weighted composite runoff coefficients (Cro) were recalculated for each sub-watershed using field-derived Cro values for eight distinct land cover classes. As shown in Figure 10, all six sub-watersheds experienced a marked increase in Cro following mining. The Lamasara sub-watershed, for instance, exhibited a post-mining Cro value of 0.439, corresponding with a 32% conversion of forest into saprolite and disposal sites. Bahopetula and Bahopenila sub-watersheds saw Cro increases of 180% and 49%, respectively, primarily due to expanded disposal and quarry activities. Even the Dampala 1 sub-watershed, which retained approximately 85% forest cover, recorded a 280% increase in Cro, reflecting the hydrologic sensitivity of the area to even modest land disturbances.

These results underscore the non-linear and cumulative nature of hydrological response to land cover change. The integration of high-resolution spatial data (Figure 8), land cover percentage shifts (Figure 9), and runoff coefficient analysis (Figure 10) demonstrates that even minor reductions in vegetative cover can result in disproportionately large increases in surface runoff. This evidence confirms that land conversion due to nickel mining substantially increases watershed-scale hydrological vulnerability, thereby amplifying the risks of erosion, sediment transport, and pollutant dispersion throughout the mining-affected catchment.

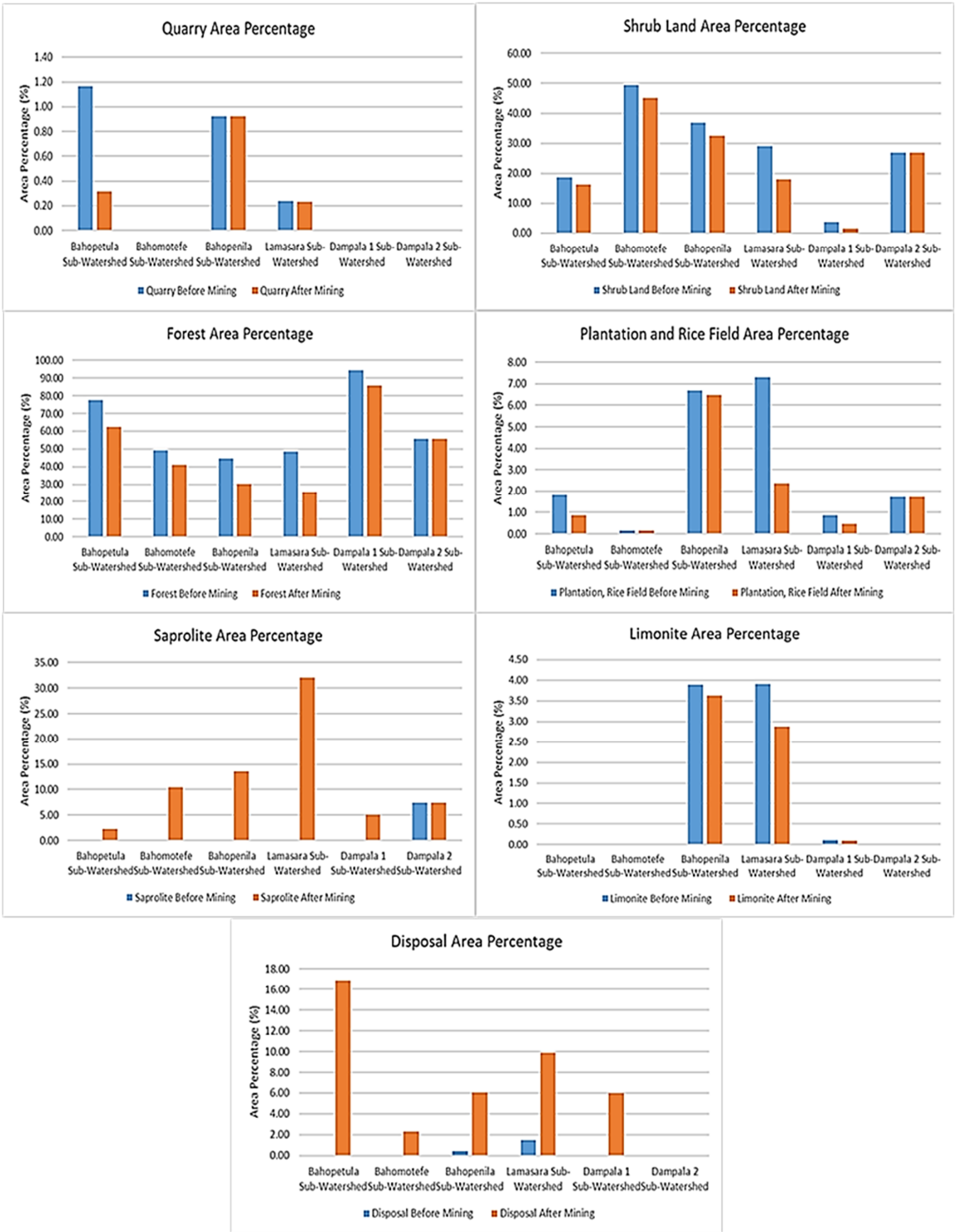

Figure 9. The land cover area percentage between pre and post nickel mining

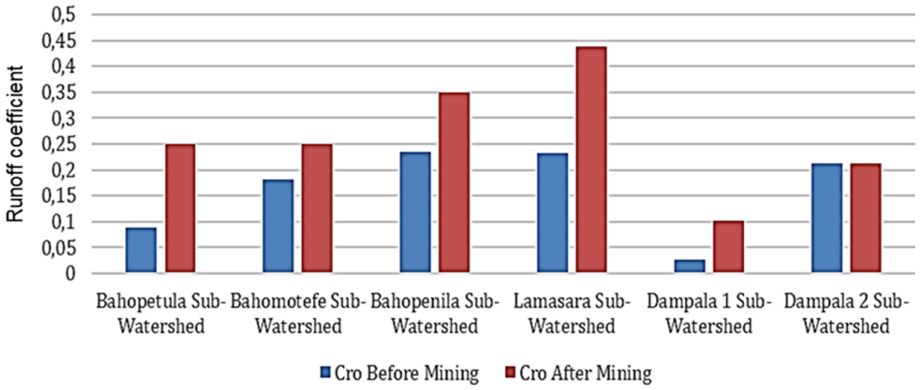

Figure 10. The comparison of runoff coefficient values of pre and post nickel mining

Nevertheless, relying solely on downstream containment is insufficient for sustainable environmental protection. A more integrated landscape-level strategy emphasizes upstream interventions, particularly revegetation and reforestation. These ecological restoration efforts enhance soil permeability, reduce runoff velocity, and increase evapotranspiration, collectively contributing to the reestablishment of natural hydrological balance in disturbed mining areas [12,13]. The revegetation process typically begins with landscaping and the incorporation of soil amendments. Effective erosion management before planting crops, along with soil additives that enhance chemical, physical, and biological conditions, is crucial in the initial phase of revegetation. The subsequent phase involves planting cover crops such as Centrosema pubescens, Calopogonium mucunoides, and Purarea javanica. These crops help protect the soil from erosion caused by rainfall while promoting nitrogen fixation to enhance soil fertility. Additionally, cultivating pioneer grasses like Vetiveria zizanioides, Cynodon dactylon, and Paspalum notatum can further mitigate erosion. Reforestation efforts may include Paraserianthes falcataria, Anthocephalus cadamba, Khaya senegalensis, and Sulawesi's native forest species, Diospyros celebica, in conjunction with the planting of cash crops such as rubber (Hevea brasiliensis), cocoa (Theobroma cacao L), coffee (Coffea spp.), and cashew (Anacardium occidentale).

A complementary and increasingly promising strategy is phytoremediation using locally adapted aquatic plants. As demonstrated by ref [63], species such as *Eichhornia crassipes* (water hyacinth), *Pistia stratiotes* (water lettuce), and *Ipomoea aquatica* (water spinach) effectively reduced Cr(VI) concentrations by over 60% within seven days in mine-affected waters. These species thrive in the acidic, nutrient-rich, and seasonally inundated environments typical of post-mining wetlands. In addition to Cr(VI) reduction, these plants contribute to lowering total suspended solids (TSS) and chemical oxygen demand (COD), reinforcing their role in integrated remediation frameworks. The success of phytoremediation, however, depends on the precise selection of species aligned with local ecological conditions, including water pH, pollutant concentrations, hydrological patterns, and sunlight availability. When strategically combined with structural runoff controls, phytoremediation enhances the functionality and resilience of treatment wetlands, transforming them into multifunctional systems that can filter pollutants, stabilize hydrological regimes, and deliver a range of broader ecosystem services.

Overall, integrating spatial land cover change analysis with empirical hydrological assessments and layered runoff control strategies offers a scientifically robust and ecologically sustainable approach to managing the hydrological impacts of nickel mining. By addressing both site-level processes and watershed-scale interactions comprehensively, this holistic framework advances best practices for post-mining restoration and long-term environmental resilience. Furthermore, to prevent and control environmental issues, nickel mining should implement an environmental impact assessment (EIA) approach to enhance sustainability. To be more comprehensive, EIA can be conducted using the mathematical and Fuzzy Delphi Folchi models [7,64].

4. Conclusions

This study presents a comprehensive evaluation of the hydrological and geochemical impacts resulting from nickel mining activities in Central

Sulawesi, Indonesia. Through the integration of field-based erosion and infiltration measurements with spatial land cover change analysis at the watershed scale, the findings demonstrate that land cover disturbance—particularly the expansion of saprolite and disposal sites—substantially increases surface runoff, sediment load, and Cr(VI) mobilization. The disposal, quarry, and saprolite sites exhibited the highest runoff coefficients and sediment loads, confirming their critical role in amplifying watershed-scale hydrological vulnerability.

Recalculation of composite runoff coefficients before and after mining revealed significant increases across all sub-watersheds, with the Lamasara and Bahopetula watersheds experiencing the most pronounced hydrological transformation. These findings highlight the importance of integrating site-specific field data with spatial modeling to assess the cumulative environmental effects of mining operations accurately.

To mitigate these impacts, this study supports the implementation of a dual-strategy framework that combines end-of-pipe treatments—such as sedimentation ponds and chemical remediation—with integrated, land-based approaches, including revegetation and phytoremediation. The application of native aquatic species, such as Eichhornia crassipes, has shown promise in reducing Cr(VI) and improving water quality in post-mining landscapes. This holistic approach offers a pathway toward sustainable mine closure planning, restoration of watershed functionality, and long-term environmental resilience in tropical mining sites.

Conflicts of interest

The authors have no conflicts of interest that could be declared relevant to the content of this article.

Funding

This research has received funding from VALE Indonesia under the Grant agreement No. 4600075320.

Acknowledgments

We sincerely thank Vale Indonesia for the generous financial support of this research. We would also like to thank Ms Rizki Pratiwi, Mr Amir Mahumud, and Mr Emil from VALE Indonesia for their support, cooperation, and assistance throughout the field survey. The authors also thank the Centre for Technology Services of the National Research and Innovation Agency (BRIN) for their support of this research.

References

[1]. Fatimah, D. Y., Her Krissanto, J. Y., Pamunga, M. N. A., & Nugroho, R. P. (2023). Nickel as a strategic mineral and its potential resources in X-Field, North Konawe, southeast Sulawesi, Indonesia. *Journal of Applied Geology*, *8*(2), 85. https://doi.org/10.22146/jag.78116.

[2]. Van der Ent, A., Baker, A. J. M., van Balgooy, M. M. J., & Tjoa, A. (2013). Ultramafic nickel laterites in Indonesia (Sulawesi, Halmahera): Mining, nickel hyperaccumulators and opportunities for phytomining. *Journal of Geochemical Exploration, 128,* 72–79. https://doi.org/10.1016/j.gexplo.2013.01.009.

[3]. Monirul Islam, M., Sohag, K., Mamman, S. O., & Herdhayinta, H. (2023). Response of Indonesian mineral supply to global renewable energy generation: Analysis based on gravity model approach. *Geoscience Frontiers*, *15*(4), 1–14. https://doi.org/10.1016/j.gsf.2023.101658.

[4]. Heijlen, W., & Duhayon, C. (2024). An empirical estimate of the land footprint of nickel from laterite mining in Indonesia. *Extractive Industries and Society*, *17,* 1–10. https://doi.org/10.1016/j.exis.2024.101421

[5]. Hudayana, B., Suharko., & Widyanta, A. B. (2020). Communal violence as a strategy for negotiation: Community responses to nickel mining industry in Central Sulawesi, Indonesia. *Extractive Industries and Society,* *7*(4), 1547–1556. https://doi.org/10.1016/j.exis.2020.08.012.

[6]. Agboola, O., Babatunde, D. E., Isaac Fayomi, O. S., Sadiku, E. R., Popoola, P., Moropeng, L., Yahaya, A., & Mamudu, O. A. (2020). A review on the impact of mining operation: Monitoring, assessment and management. *Results in Engineering*, *8,* 1–23. https://doi.org/10.1016/j.rineng.2020.100181.

[7]. Ataei, M., Tajvidi Asr, E., Khalokakaie, R., Ghanbari, K., & Mohammadi, M. R. T. (2016). Semi-quantitative environmental impact assessment and sustainability level determination of coal mining using a mathematical model. *Journal of Mining & Environment,* *7*(2): 185-193. https://doi.org/10.22044/jme.2016.515.

[8]. Prematuri, R., Turjaman, M., Sato, T., & Tawaraya, K. (2020). The impact of nickel mining on soil properties and growth of two fast-growing tropical trees species. *International Journal of Forestry Research*, *19,* 1–9. https://doi.org/10.1155/2020/8837590.

[9]. Ranjan, A. K., Parida, B. R., Dash, J., & Gorai, A. K. (2022). Quantifying the impacts of opencast mining on vegetation dynamics over eastern India using the long-term Landsat-series satellite dataset. *Ecological Informatics*, *71*, 1–17. https://doi.org/10.1016/j.ecoinf.2022.101812.

[10]. Sellier, V., Navratil, O., Laceby, J. P., Allenbach, M., Lefèvre, I., & Evrard, O. (2021). Reconstructing the impact of nickel mining activities on sediment supply to the rivers and the lagoon of South Pacific Islands: Lessons learnt from the Thio early mining site (New Caledonia). *Geomorphology*, *372,* 1–15. https://doi.org/10.1016/j.geomorph.2020.107459.

[11]. Worlanyo, A. S., & Jiangfeng, L. (2021). Evaluating the environmental and economic impact of mining for post-mined land restoration and land-use: A review. *Journal of Environmental Management, 279*, 1–16. https://doi.org/10.1016/j.jenvman.2020.111623.

[12]. Mabuda, M. O., Shoko, C., Dube, T., & Mazvimavi, D. (2024). An analysis of the effects of changes in land use and land cover on runoff in the Luvuvhu catchment, South Africa. *Remote Sensing Applications: Society and Environment*, *33*, 1–14. https://doi.org/10.1016/j.rsase.2024.101144.

[13]. Affessa, G. M., Belew, A. Z., Tenagashaw, D. Y., & Tamirat, D. M. (2022). Land Use/Cover Change Impacts on Hydrology Using SWAT Model on Borkena Watershed, Ethiopia. Water *Water Conservation Science and Engineering*, *7*(1), 55–63. https://doi.org/10.1007/s41101-022-00128-1.

[14]. Delina, R. E., Arcilla, C., Otake, T., Garcia, J. J., Tan, M., & Ito, A. (2020). Chromium occurrence in a nickel laterite profile and its implications to surrounding surface waters. *Chemical Geology*, *558*, 1–14. https://doi.org/10.1016/j.chemgeo.2020.119863.

[15]. Mitchell, S. B., West, J. R., & Guymer, I. (2007). Dissolved-Oxygen/Suspended-Solids Concentration Relationships in the Upper Humber Estuary. *Water and Environmental Journal, 13*(5), 327–337. https://doi.org/DOI:10.1111/j.1747-6593.1999.tb01057.x.

[16]. Zhu, W., Kunz, J., Brunson, E., Barnhart, C., Brown, H., McMurray, S., Roberts, A. D., Shulse, C., Trauth, K., Wang, B., Steevens, J. A., & Deng, B. (2023). Impacts of acute and chronic suspended solids exposure on juvenile freshwater mussels. *Science of the Total Environment*, *905,* 1–12. https://doi.org/10.1016/j.scitotenv.2023.167606.

[17]. Majalis, A. N., Wicaksono, N., Novitasari, Y., Permatasari, N. and Pratiwi, R. (2022). Pengolahan kromium(vi) pada air limbah pertambangan bijih nikel menggunakan besi(ii) yang diperoleh dari slag nikel. *Jurnal Teknologi Mineral Dan Batubara*, *18*(3), 177–191. https://doi.org/10.30556/jtmb.Vol18.No3.2022.1314.

[18]. Iyer, M., Anand, U., Thiruvenkataswamy, S., Babu, H. W. S., Narayanasamy, A., Prajapati, V. K., Tiwari, C. K., Gopalakrishnan, A. V., Bontempi, E., Sonne, C., Barceló, D., & Vellingiri, B. (2023). A review of chromium (Cr) epigenetic toxicity and health hazards. *Science of the Total Environment, 882*, 1–12. https://doi.org/10.1016/j.scitotenv.2023.163483.

[19]. Azeez, N. A., Dash, S. S., Gummadi, S. N., & Deepa, V. S. (2021). Nano-remediation of toxic heavy metal contamination: Hexavalent chromium [Cr(VI)]. *Chemosphere, 266*, 1–11. https://doi.org/10.1016/j.chemosphere.2020.129204.

[20]. Ruth, A. U., Kelechi, I. K., Timothy, C. O., & Ike-Amadi, A. C. (2014). Application of Kostiakov's Infiltration Model on the Soils of Umudike, Abia State-Nigeria. *American Journal of Environmental Engineering,* 2014(1), 1–6. https://doi.org/10.5923/j.ajee.20140401.01.

[21]. Yang, M., Zhang, Y., & Pan, X. (2020). Improving the Horton infiltration equation by considering soil moisture variation. *Journal of Hydrology*, *586,* 1–10. https://doi.org/10.1016/j.jhydrol.2020.124864.

[22]. Wang, X., Sample, D. J., Pedram, S., & Zhao, X. (2017). Performance of two prevalent infiltration models for disturbed urban soils. *Hydrology Research*, *48*(6), 1520–1536. https://doi.org/10.2166/nh.2017.217.

[23]. Ruggenthaler, R., Meißl, G., Geitner, C., Leitinger, G., Endstrasser, N., & Schöberl, F. (2016). Investigating the impact of initial soil moisture conditions on total infiltration by using an adapted double-ring infiltrometer. *Hydrological Sciences Journal*, *61*(7), 1263–1279. https://doi.org/10.1080/02626667.2015.1031758.

[24]. Duiker, S. W., Flanagan, D. C., & Lal, R. (2001). Erodibility and infiltration characteristics of five major soils of southwest Spain. *Catena, 45*(2): 103–121. https://doi.org/10.1016/S0341-8162(01)00145-X.

[25]. Robertson, W. M., & Sharp, J. M. (2015). Estimates of net infiltration in arid basins and potential impacts on recharge and solute flux due to land use and vegetation change. *Journal of Hydrology*, *522*, 211–227. https://doi.org/10.1016/j.jhydrol.2014.11.081.

[26]. Seiwa, K., Kunii, D., Masaka, K., Hayashi, S., & Tada, C. (2021). Hardwood mixture enhances soil water infiltration in a conifer plantation. *Forest Ecology and Management*, *498,* 1–9. https://doi.org/10.1016/j.foreco.2021.119508.

[27]. Panggabean, H., & Surono. (2011). Tektono-Stratigrafi Bagian Timur Silawesi. *Jurnal Sumberdaya Geologi*, *21*(5), 239–48. https://doi.org/10.33332/jgsm.geologi.v21i5.150.

[28]. Hasria, Hasan, E. S., Deniyatno, Salihin, L. M. I., & Asdiwan. (2020). Characteristics of Ultramafic Igneous Rock Ofiolite Complex in Asera District, North Konawe Regency Southeast Sulawesi Province. *Journal of Geoscience, Engineering, Environment, and Technology*, *5*(3), 121–126. https://doi.org/10.25299/jgeet.2020.5.3.4113.

[29]. Al Ghiffari. M. R., Nugroho. D., Ramadhan. R., Noor. M. R., Wicaksono. N., & Agustan. (2024). The Utilization of LiCSBAS for Deformation Monitoring in Geresa Segment of Matano Fault, Central Sulawesi,

Indonesia. *Journal of Geoscience, Engineering, Environment, and Technology*, *9*(1), 28–37. https://doi.org/10.25299/jgeet.2024.9.1.14212.

[30]. Irzon, R., & Abdullah, B. (2018). Element mobilization during weathering process of ultramafic complex in North Konawe Regency, southeast Sulawesi based on a profile from Asera. *Indonesian Journal on Geoscience*, *5*(3), 277–290. https://doi.org/10.17014/ijog.5.3.277-290.

[31]. Nugrahini A, Handayana F., & Wijayantia H. D. K. (2022). Karakteristik Profil Nikel Laterit Blok X, Daerah Siumbatu, Kecamatan Bahodopi, Kabupaten Morowali, Provinsi Sulawesi Tengah. *Prosiding Nasional Teknologi Industri dan Informasi XVII Tahun 2022 (ReTII),* 683–691. http://journal.itny.ac.id/index.php/ReTII

[32]. Puspita, R., Ninasafitri, N., & Ente, Moh. R. (2022). Characteristics of Ultramafik Rock and Nickel Laterite Distribution in Siuna Area, Pagimana, Banggai, Central Sulawesi. *Jurnal Geocelebes, 6*(1), 93–107. https://doi.org/10.20956/geocelebes.v6i1.18523.

[33]. Sharma, P., Singh, S. P., Parakh, S. K., & Tong, Y. W. (2022). Health hazards of hexavalent chromium (Cr (VI)) and its microbial reduction. *Bioengineered, 13*(3): 4923–4938. https://doi.org/10.1080/21655979.2022.2037273.

[34]. Christita, M., & Iwanuddin. (2018). The Ability of Hexavalen Chromium (Cr6+) Reduction by Bacteria Isolated from Nickel Post Mining Soil at East Halmahera. *Proceedings of IUFRO - INAFOR Joint Conference*, 11–9. https://www.researchgate.net/publication/327666394.

[35]. Abdourhamane Toure, A., Rajot, J. L, Garba, Z., Marticorena, B., Petit, C., & Sebag, D. (2011). Impact of very low crop residues cover on wind erosion in the Sahel. *Catena, 85*(3), 205–214. https://doi.org/10.1016/j.catena.2011.01.002.

[36]. Hudson, N. W. (1993). *Fild Measurement of Soil Erosion and Runoff*, FAO of UN, Rome. https://www.fao.org/4/t0848e/t0848e00.htm.

[37]. Sangüesa, C., Arumí, J., Pizarro, R., & Link, O. (2010). A Rainfall Simulator for The in Situ Study of Superficial Runoff and Soil Erosion. *Journal of Agriculturan Research, 70*(1), 178–182. http://dx.doi.org/10.4067/S0718-58392010000100019.

[38]. Rauber, L. R., Mallman, M. S., Reinert, D. J., Pires, F. S., de Vargas, F., & Gubiani, P. I. (2024). Automatic measurement of water infiltration into the soil. *Revista Brasileira de Ciencia Do Solo*, *48*. e0230078. https://doi.org/10.36783/18069657rbcs20230078.

[39]. Zhang, J., & Li, S. (2020). Surface-positioned double-ring to improve traditional infiltrometer for measuring soil infiltration. *Soil Research, 58*(3), 314–321. https://doi.org/10.1071/SR19260.

[40]. Drescher, G. L., Slaton, N. A., Ahmad, U., Smartt, A. D., Roberts, T. L., & Gbur, E. E. (2024). Soil moisture and probe characteristics affect core integrity and soil test results. *Soil Science Society of America Journal*, *88*(4), 1216–1233. https://doi.org/10.1002/saj2.20696.

[41]. Wang, Y., Ma, Z., Li, D., Hou, G., & Zheng, J. (2024). Infiltration Characteristics and Hydrodynamic Parameters in Response to Topographic Factors in Bare Soil Surfaces, Laboratory Experiments Based on Cropland Fields of Purple Soil in Southwest China. *Agriculture (Switzerland)*, *14*(10), 1820. https://doi.org/10.3390/agriculture14101820.

[42]. Descroix, L., & Amogu, O. (2012). *Consequences of land use changes on hydrological functioning*. InTechOpen eBooks. https://doi.org/10.5772/34839.

[43]. Cerdan, O., Govers, G., Le Bissonnais, Y., Van Oost, K., Poesen, J., & Saby, N. (2010). Rates and spatial variations of soil erosion in Europe: A study based on erosion plot data. *Geomorphology, 122*, 167–77. https://doi.org/10.1016/j.geomorph.2010.06.011.

[44]. García-Ruiz, J. M., Beguería, S., Nadal-Romero, E., González-Hidalgo, J. C., Lana-Renault, N., & Sanjuán, Y. (2015). A meta-analysis of soil erosion rates across the world. *Geomorphology, 239,* 160–173. https://doi.org/10.1016/j.geomorph.2015.03.008.

[45]. Grismer, M. (2012). Standards vary in studies using rainfall simulators to evaluate erosion. *California Agriculture, 66*(3), 102–107. https://doi.org/10.3733/ca.v066n03p102.

[46]. Sulianto, M. E, Widodo, S., & Novita, E. (2014). Infiltration Constant Determination of Modified Kostiakov Equation in Sumbersari, Kaliwates, and Pakusari District. *Berkah Ilmiah TEKNOLOGI PERTANIAN*, *1*(1), 1–4.

[47]. Bahddou, S., Otten, W., Whalley, W. R., Shin, H. C., El Gharous, M., & Rickson, R. J. (2023). Changes in soil surface properties under simulated rainfall and the effect of surface roughness on runoff, infiltration and soil loss. *Geoderma*, *431,* 1–12. https://doi.org/10.1016/j.geoderma.2023.116341.

[48]. Li, J., Wu, L., Chen, L., Zhang, J., Shi, Z., Ling, H., Cheng, C., Wu, H., Butler, A. D., Zhang, Q., Arslan, Z., Pierce, E. M., Su, Y., & Han, F. X. (2024). Effects of slopes, rainfall intensity and grass cover on runoff loss of mercury from floodplain soil in Oak Ridge TN: A laboratory pilot study. *Geoderma, 441*, 1–11. https://doi.org/10.1016/j.geoderma.2023.116750.

[49]. Asempah, M., Shisanya, C. A., & Schütt, B. (2024). Modeling of soil erosion risk in a typical tropical savannah landscape. *Scientific African*, *23,* 1–20. https://doi.org/10.1016/j.sciaf.2023.e02042.

[50]. Kayet, N., Pathak, K., Chakrabarty, A., & Sahoo, S. (2018). Evaluation of soil loss estimation using the RUSLE model and SCS-CN method in hillslope mining areas. *International Soil and Water Conservation*

Research, *6*(1), 31–42. https://doi.org/10.1016/j.iswcr.2017.11.002.

[51]. Tian, G., Li, X., He, F., Guo, S., Wang, Y., Li, Y., Zong, W., & Liu, R. (2023). Molecular toxicity of Cr(III) and Cr(VI) to defensive protein lysozyme and their differential mechanisms. *Journal of Molecular Liquids*, *390,* 1–9. https://doi.org/10.1016/j.molliq.2023.123151.

[52]. Pokhrel, G.R., & Pokhrel, G. (2022). The effect of Chromium on Human-Health: A Review. *BMC Journal of Scientific Research, 5*(1), 27-35. https://doi.org/10.3126/bmcjsr.v5i1.50669.

[53]. Shin, D. Y., Lee, S. M., Jang, Y., Lee, J., Lee, C. M., & Cho, E. M. (2023). Adverse Human Health Effects of Chromium by Exposure Route: A Comprehensive Review Based on Toxicogenomic Approach. *International Journal of Molecular Sciences, 24*(4), 3410. https://doi.org/10.3390/ijms24043410.

[54]. Faisal, M., Hameed, A., & Hasnain, S. (2005). Chromium-resistant bacteria and cyanobacteria: Impact on Cr(VI) reduction potential and plant growth. *Journal of Industrial Microbiology and Biotechnology*, *32*, 615–621. https://doi.org/10.1007/s10295-005-0241-2.

[55]. Karimi-Maleh, H., Ayati, A., Ghanbari, S., Orooji, Y., Tanhaei, B., & Karimi, F. (2021). Recent advances in removal techniques of Cr(VI) toxic ion from aqueous solution: A comprehensive review. *Journal of Molecular Liquids,* 329, 115062. https://doi.org/10.1016/j.molliq.2020.115062.

[56]. Sharma, A., Kapoor, D., Wang, J., Shahzad, B., Kumar, V., & Bali, A. S. (2020). Chromium bioaccumulation and its impacts on plants: An overview. *Plants, 9*(1). https://doi.org/10.3390/plants9010100.

[57]. Yu, Z., Xu, S. F., Zhao, J. L., Zhao, L., Zhang, A. Z., & Li, M. Y. (2021). Toxic effects of hexavalent chromium (Cr6+) on bioaccumulation, apoptosis, oxidative damage and inflammatory response in Channa asiatica *Environmental Toxicology and Pharmacology*, *87,* 103725. https://doi.org/10.1016/j.etap.2021.103725.

[58]. Aprisal, Istijono, B., Ophiyandri, T., & Nurhamidah. (2019). A study of the quality of soil infiltration at the downstream of Kuranji River, Padang City. *International Journal of GEOMATE, 16*(56), 16–20. https://doi.org/10.21660/2019.56.4530.

[59]. Cleophas, F., Isidore, F., Musta, B., Mohd Ali, B. N., Mahali, M., Zahari, N. Z., & Bidin, K. (2022). Effect of soil physical properties on soil infiltration rates. *Journal of Physics: Conference Series*, *2314*(1), 1–6. https://doi.org/10.1088/1742-6596/2314/1/012020.

[60]. de Almeida, W. S., Panachuki, E., de Oliveira, P. T. S., da Silva Menezes, R., Sobrinho, T. A., & de Carvalho, D. F. (2018). Effect of soil tillage and vegetal cover on soil water infiltration. *Soil and Tillage Research*, *175*, 130–138. https://doi.org/10.1016/j.still.2017.07.009.

[61]. Feng, Z., Hu, Z., Zhang, X., Zhang, Y., Cui, R., & Lu, L. (2023). Integrated Mining and Reclamation Practices Enhance Sustainable Land Use: A Case Study in Huainan Coalfield, China. *Land*, *12*(11), 1994. https://doi.org/10.3390/land12111994.

[62]. Zotter, K. A. (2004). "End-of-pipe" versus "process-integrated" water conservation solutions: A comparison of planning, implementation and operating phases. *Journal of Cleaner Production*, *12*(7), 685–695. https://doi.org/10.1016/S0959-6526(03)00115-X.

[63]. Permatasari, N. V., Abidin, F., Azmi, M. U., Novitasari, Y., & Hapid, A. (2024). Phytoremediation of Hexavalent Chromium Using Aquatic Plants in Nickel Mine Waste. *EKSPLORIUM*, *44*(2), 81. https://doi.org/10.55981/eksplorium.2023.6927.

[64]. Saffari, A., Ataei, M., Sereshki, F., & Naderi, M. (2019). Environmental impact assessment (EIA) by using the Fuzzy Delphi Folchi (FDF) method (case study: Shahrood cement plant, Iran). *Environment, Development and Sustainability*, *21*(2), 817–860. https://doi.org/10.1007/s10668-017-0063-1.

انجمن مهندسی معدن ایران
نشریه مهندسی معدن و محیط زیست
نشانی نشریه: www.jme.shahroodut.ac.ir
دانشگاه صنعتی شاهرود

کاهش اثرات زیست محیطی فعالیت معدن نیکل – مطالعه موردی در سولاوسی مرکزی، اندونزی

آسپ نورحمت مجالس[۱]*، محمد رزاق ال گیفاری[۲]، آر عارف سوریانگارا[۲]، ام رفعت نور[۳]، راچمت رمضان[۴]، و نوویارسو ویکاسونو[۳]

۱. مرکز تحقیقات شیمی، آژانس ملی تحقیقات و نوآوری، تانگرانگ-بانتن جنوبی، اندونزی
۲ .مرکز تحقیقات محیط زیست و فناوری های پاک، آژانس ملی تحقیقات و نوآوری، جنوب تانگرنگ-بانتن، اندونزی
۳ .مرکز تحقیقات فناوری معدنی، آژانس ملی تحقیقات و نوآوری، Tanjung Bintang-Lampung، اندونزی
۴. آژانس ملی تحقیقات و نوآوری، جاکارتا، اندونزی

اطلاعات مقاله

تاریخ ارسال: ۲۰۲۵/۰۵/۱۹
تاریخ داوری: ۲۰۲۵/۰۸/۰۷
تاریخ پذیرش: ۲۰۲۵/۱۱/۰۹

DOI: 10.22044/jme.2025.16265.3158

کلمات کلیدی

مدیریت اثرات زیست‌محیطی معدن
نفوذپذیری، ضریب رواناب سطحی
بار رسوب
کروم شش ظرفیتی

چکیده

اندونزی به دلیل ذخایر عظیم نیکل خود، به یکی از بزرگترین سایت‌های استخراج و تولید نیکل در جهان تبدیل شده است. نیکل یک کالای معدنی با ارزش اقتصادی بالا است. با این حال، فعالیت معدنی آن در صورت عدم مدیریت صحیح می‌تواند تأثیر منفی بر محیط زیست داشته باشد. بنابراین، کاهش تأثیر استخراج نیکل ضروری است. این تحقیق آزمایش‌های فرسایش و نفوذ را در مکان‌های مختلف در سایت‌های پیش از استخراج نیکل انجام داده است تا تأثیر زیست‌محیطی فعالیت استخراج نیکل را کاهش دهد. آزمایش‌های فرسایش با استفاده از یک شبیه‌ساز باران با پنج نازل در یک قطعه آزمایشی ۱۲.۵ متر مربعی انجام شد. آزمایش‌های نفوذ با استفاده از یک نفوذسنج حلقه‌ای دوگانه انجام شد. نتایج نشان می‌دهد که ضرایب رواناب سطحی برای سایت‌های دفع زباله، لیمونیت، ساپرولیت و معدن سنگ بیشتر از سایت‌های دارای پوشش گیاهی مانند علفزار، کشت فلفل و جنگل بوده است. سایت ساپرولیت بالاترین بار رسوب، یعنی ۴۸۴.۳ کیلوگرم در هکتار در ساعت، و پس از آن لیمونیت و سایت کاشت فلفل، با ۲۴۳.۶ کیلوگرم در هکتار در ساعت و ۱۸۵ کیلوگرم در هکتار در ساعت، قرار داشتند. بالاترین غلظت Cr(VI)، ۰.۷ میلی‌گرم در لیتر، از سایت دفع زباله آزاد شد و پس از آن به ترتیب سایت‌های کاشت ساپرولیت، لیمونیت و فلفل با غلظت‌های ۰.۵۶، ۰.۰۶ و ۰.۰۶ میلی‌گرم در لیتر قرار داشتند. معادله نفوذ به‌دست‌آمده از هر سایت نشان می‌دهد که احیای پوشش گیاهی می‌تواند رواناب را به طور قابل توجهی کاهش دهد. بنابراین، علاوه بر تصفیه انتهای لوله، احیای پوشش گیاهی نیز باید در اولویت قرار گیرد تا تأثیر فعالیت‌های استخراج نیکل کاهش یابد.

نویسنده مسئول مکاتبات: najmeddinali@ut.ac.ir (ن. ر. مجالس)